From Source Structure to Spectral Profiles: Generation Mechanisms and Observable Readouts in the Canonical Spectral-Curvature Framework

Jeremy Rodgers

DOI: 10.5281/zenodo.23912447

everythingequation.com

3 November 2026

Abstract

Recurring spectral-ratio profiles can arise through explicit constructions that retain different physical and mathematical information. We develop three source-to-readout mechanisms: the radial-shell organization of a finite hydrogen coupling graph, Gaussian exchange on specified spatial preparations, and the joint angular and outgoing radial boundary problem for Kerr resonances. For hydrogen, an exact same-shell spectrum, a source-derived minimum, signed local self-energies and a radial moment bound with orthogonal external-shell subtraction control the finite construction and recover all 45 original ratio-window counts numerically. For spatial networks, a deterministic degree-to-spectrum theorem transfers Gaussian preparation laws to limiting ratio distributions and quantifies coordinate and deletion uncertainty. For Kerr, continuation with overtone-label diagnostics and radial-depth refinement reconstructs the full 540-label native profile. These mechanisms enter the Canonical Spectral-Curvature Framework through declared forms, metrics, retained sectors and readouts; the outgoing pole problem requires an explicit enlargement beyond the commuting positive-carrier subclass. Exact homometric examples and response-reconstruction theorems show which source distinctions pooled ratios discard and which calibrated observations restore them. The resulting account explains concrete generation routes and supplies discriminating observations without identifying their recurrence with one shared microscopic law.

Contents

1 The source-selection problem **2**

2 Realizations, readouts and retained information **3**
2.1 The mathematical interface to CSCF and Shadow Theory 3
2.2 The original finite observable 4

3 Hydrogen: radial shells, normalization and finite profile control **4**
3.1 The finite source and its exact radial data 4
3.2 An exact same-shell spectrum 5
3.3 Adjacent shells, the minimum and signed cancellation 6
3.4 Signed shell self-energies and a radial convergence bound 8
3.5 Returning the bound to all original counts 9
3.6 Cutoff concentration and the informative finite tail 10

4 A physical dipole carrier and an operational loss readout **10**
4.1 Angular factors and the equilibrium metric . . . 10
4.2 Loss mixtures realize the logarithmic readout . . . 12

5 Spatial preparation and kernel-mass heterogeneity **12**
5.1 A conditional Gaussian-exchange realization . . . 12
5.2 A finite degree-to-spectrum theorem . . . 13
5.3 A preparation law generates a ratio distribution . . . 13
5.4 Extraction uncertainty and source-image scope . . . 14

6 Kerr: joint angular and outgoing radial dynamics **15**
6.1 The native selection and the source boundary problem . . . 15
6.2 Finite angular control and barrier shape . . . 16
6.3 Branch identity and the complete numerical return . . . 16
6.4 The boundary-pole extension of the carrier picture . . . 17

7 What ratio profiles identify, and what response adds **17**
7.1 An exact homometric obstruction . . . 17
7.2 Static elimination is not dynamical identification . . . 18
7.3 Calibrated response as a constructive completion . . . 18

8 A connected source-to-readout account **19**
8.1 Discriminating observations . . . 19
8.2 Evidence boundaries and reproducibility . . . 20

9 Conclusion **20**

A Exact radial evaluation and numerical conventions **20**

B Homogeneous ring preparation **21**

C Verification scope and generated numerical tables **21**

1 The source-selection problem

Finite spectral profiles compare systems after several consequential transformations. A source law supplies an operator or boundary problem; a preparation selects accessible states; a readout transforms the retained spectrum; and a pair statistic pools the resulting values. Similarity at the last stage can reflect structure at any of these stages. An explanatory account therefore needs constructions that reach the original statistic from specified source data, together with estimates that survive the transformations.

This paper continues two complementary studies. The spectral investigation [1] records recurrence, conditional-reference discrimination, robustness and diagnostic limits for a hydrogen radial graph, gravitational Kerr damping readouts and image-derived Gaussian graphs. The Canonical Spectral-Curvature Field (CSCF) paper [2] establishes a common-carrier architecture for complementary dissipative and coherent responses, and locates the finite ratio observable in its modular calculus. The present work supplies generation mechanisms and quantitative controls. Its main mathematical contribution is the passage from radial rules, spatial preparation and outgoing boundary conditions to the retained finite profiles, rather than another representation of a profile already known.

Three constructions organize the argument. Hydrogen supplies an unusually explicit finite source: normalized Coulomb radial functions determine every squared edge weight rationally,

same-shell chains have a closed spectrum, and omitted shells can be separated according to their effects on the minimum and the bulk. Spatial networks supply a different explanatory route: a Gaussian interaction kernel makes the Laplacian spectrum close to the distribution of kernel mass at prepared sites. Kerr supplies a joint frequency-and-damping law through an open boundary problem. Its poles cannot generally be replaced by a nondecreasing frequency symbol of a damping-only carrier.

The evidence has several levels. Finite identities and conditional theorems are proved below. Exact rational computations verify scalar radial budgets, stored edges and independent finite fixtures. Matrix inverses, gaps, eigenvalues, inertia evaluations and resonance continuation use disclosed numerical arithmetic. Repeating the same implementation establishes repeatability; separate eigensolvers and independently formulated fixtures provide additional numerical checks. Neither class is an atomic or image-formation experiment. This distinction determines the strength of the conclusions while allowing the completed constructions to be used directly.

2 Realizations, readouts and retained information

2.1 The mathematical interface to CSCF and Shadow Theory

The useful source-to-readout chain is

$$\begin{gathered}\text{source law and preparation} \longrightarrow \text{metric, carrier or boundary poles} \\ \longrightarrow \text{retained readout} \longrightarrow \text{pair profile.}\end{gathered} \tag{1}$$

Each arrow requires its own data. A geometric support does not by itself specify mobility, physical time, an energy form or a detector. In Shadow Theory [3–5], descent through a readout is a target-relative condition: a target can be recovered exactly only when it is constant on the readout's fibres. Geometric realization additionally requires compatible metric, domain and boundary data. Exact projection of a dynamical source retains unresolved initial-state and memory terms unless an invariance condition removes them. We use these statements as mathematical constraints on the arrows in (1), not as substitutes for the Coulomb, Gaussian or Kerr laws.

In a finite CSCF realization a declared Hermitian nonnegative form Q on a Hilbert space has representative $K \geq 0$. For a graph with nonnegative symmetric weights,

$$Q(z) = z^* L z = \sum_{i<j} W_{ij} |z_i - z_j|^2, \qquad L = \operatorname{diag}(W\mathbf{1}) - W. \tag{2}$$

The quadratic potential $Q/2$ has this Hessian in its stated metric. With an admissible bounded real nondecreasing symbol h, vanishing at zero and with $h(K) \neq 0$ for a nonzero carrier, the paired mathematical responses are

$$S_t = e^{-tK}, \qquad C = h(K), \qquad U_s = e^{-\mathrm{i}sC}. \tag{3}$$

The common carrier is shared by these two responses *within a realization*. Different domains do not acquire an identical matrix from this assertion. Physical identification of K requires an energy and mobility, or an equivalent kinetic derivation. Physical identification of C requires the nominated reactive law and the same modal coordinates.

For example, linearizing $\dot{q} = -M(q)\nabla F(q)$ at a stationary point with $M_* > 0$ and $H = \operatorname{Hess} F \geq 0$, the coordinate $y = M_*^{-1/2}(q - q_*)$ satisfies

$$\dot{y} = -Ky, \qquad K = M_*^{1/2} H M_*^{1/2}. \tag{4}$$

The product of mobility and curvature has inverse-time units. A Hessian alone need not have those units. A reversible population generator Q_M with stationary probability π instead gives $K = -D_\pi^{1/2} Q_M D_\pi^{-1/2}$; detailed balance makes it selfadjoint and its stationary vector is $\sqrt{\pi}$. These metric distinctions will be essential for the dipole-bath carrier.

2.2 The original finite observable

For $m \geq 2$, let $v_1, \ldots, v_m > 0$ be the retained labelled readout values, including multiplicities. For an eligible-ratio set B_r with nonzero exposure define

$$E = \{(i,j) : i \neq j,\ v_i/v_j \in B_r\}, \qquad N_R = |E|. \tag{5}$$

The fifteen comparison coordinates, in their fixed order, are

$$(\varphi, \varphi^{-1}, \varphi^2, \sqrt{2}, \sqrt{3}, \sqrt{5}, \pi, \pi/2, \pi/10, e, e^{-1}, \log 2, j_{0,1}, 3/13, 1/7), \tag{6}$$

where $\varphi = (1+\sqrt{5})/2$ and $j_{0,1}$ is the first positive zero of J_0. For each $\epsilon \in \{0.03, 0.01, 0.005\}$,

$$h_k = \sum_{(i,j)\in E} \mathbf{1}_{[c_k(1-\epsilon), c_k(1+\epsilon)]}(v_i/v_j), \qquad p_k = h_k/N_R. \tag{7}$$

All windows are closed. Hydrogen and spatial networks have no additional ratio filter, so $N_R = m(m-1)$. Kerr uses the open eligibility interval $B_r = (0.05, 5)$. SUM adds all h_k, retaining overlaps. UNION counts each pair in the union of the windows once. Neither can silently replace the other.

Writing $u_i = \log v_i$, the complete nonself log-ratio measure is

$$\nu = \frac{1}{m(m-1)} \sum_{i\neq j} \delta_{u_i - u_j} = \frac{m}{m-1} \mu * \check{\mu} - \frac{1}{m-1}\delta_0, \qquad \mu = \frac{1}{m}\sum_i \delta_{u_i}. \tag{8}$$

Here $\check{\mu}$ is the reflection of μ under $u \mapsto -u$. Only labelled self-pairs are removed. Equal-valued distinct modes remain. Let V be the positive retained readout operator with eigenvalues v_i. On its Hilbert–Schmidt matrix space, $\rho = V/\operatorname{tr} V$ with eigenvalues $v_i/\sum_j v_j$ gives the modular operator $X \mapsto \rho X \rho^{-1}$ with eigenvalues v_i/v_j. Its logarithm is $[\log V, \cdot]$. This exact bridge [2] places the statistic within the declared spectral calculus; it does not turn an image graph into a measured quantum state or supply a physical clock for the log-difference conjugate variable.

The constants in (6) remain comparison coordinates. The preceding study's paired-library fraction 0.2339 failed its frozen 0.05 criterion. Generation of the measured vector therefore carries no new inference of unique library privilege. Likewise, the 45 coordinates, a complete ratio measure, a scalar spectrum, an operator-valued readout and a calibrated temporal response are different inputs to an inverse problem.

3 Hydrogen: radial shells, normalization and finite profile control

3.1 The finite source and its exact radial data

The empirical construction has vertices (n, ℓ), $1 \leq n \leq 30$, $0 \leq \ell < n$. There is one vertex per radial state, giving 465 vertices, rather than an expansion over magnetic states. With $a_0 = 1$, normalized Coulomb radial functions are

$$R_{n\ell}(r) = \frac{2}{n^2}\sqrt{\frac{(n-\ell-1)!}{(n+\ell)!}} e^{-r/n} (2r/n)^\ell L_{n-\ell-1}^{2\ell+1}(2r/n). \tag{9}$$

For $|\ell - k| = 1$ set $W_{n\ell,mk} = |\int_0^\infty R_{n\ell}(r) R_{mk}(r) r^3\, dr|^2$, and otherwise set the weight to zero. The graph Laplacian is $L = D - W$. Its 8,990 undirected edges include all 435 same-principal-shell links. The positive sector has dimension 464, exposure 214832, and native readout

$$v_i = \log(1 + \lambda_i/a), \qquad a = \lambda_{\min,+}(L). \tag{10}$$

The graph is not the atomic energy Hamiltonian $E_n = -1/(2n^2)$. It is also different from the historical 78-state H12 construction, which omitted same-shell links and used absolute radial amplitudes with an $m = 0$ angular factor. No H12 value enters the calculations here.

The finite Laguerre expansion in (9) reduces each integral to a finite sum of factorials and rational powers, multiplied by a square root of a rational number. Squaring therefore gives an exact rational weight. The supplement includes that implementation, exact same-shell fixtures and checks against the stored binary64 graph. Exact regeneration verifies all 8,990 weights and bounds their individual relative rounding errors by $u = 2^{-53}$. This is an exact statement about scalar inputs; it does not certify every subsequent matrix operation.

3.2 An exact same-shell spectrum

For a fixed n, the radial recurrence gives

$$I_{n\ell,n,\ell+1} = -\frac{3}{2} n \sqrt{n^2 - (\ell+1)^2}, \qquad w_{n,\ell} = \frac{9}{4} n^2 [n^2 - (\ell+1)^2]. \tag{11}$$

These identities follow either by inserting the terminating Laguerre series or by using its three-term recurrence and orthogonality. The negative integral sign disappears in the squared construction.

Proposition 3.1 (Same-shell modes)**.** *The path on $\ell = 0, \ldots, n-1$ with weights (11) has eigenvalues*

$$\lambda^{(0)}_{n,r} = \frac{9}{4} n^2 (2r)(2r+1), \qquad r = 0, \ldots, n-1. \tag{12}$$

Proof. On nodes $j = 0, \ldots, m$, the weighted path operator

$$\mathcal{A}f(j) = (j+1)(m-j)[f(j) - f(j+1)] + j(m-j+1)[f(j) - f(j-1)]$$

preserves polynomial degree and acts on the leading term of j^k by multiplication by $k(k+1)$. The degree filtration triangularizes this $(m+1)$-dimensional operator, with distinct eigenvalues $k(k+1)$, $0 \le k \le m$. Reflection $j \mapsto m - j$ commutes with it. The eigenpolynomial of degree k has parity $(-1)^k$, because its reflected leading term has that parity and its eigenspace is one-dimensional. Set $m = 2n - 1$ and restrict to the even reflection sector. Pairing the reflected sites gives the n-node half-path with a reflecting endpoint; the central edge contributes zero. Its edge weights are $n^2 - (\ell+1)^2$ after reversing the half-path order. Thus $k = 2r$ and the factor $9n^2/4$ gives the result. □

The disconnected same-shell direct sum has 30 zero modes. Inter-shell links lift 29 of them and retain the global constant. It would change the original statistic to discard those shell-constant directions. At cutoff 30, same-shell weights carry about 76.77% of total strength; the adjacent-shell graph retains 1,276 edges and about 97.92%. These fractions explain the leading organization but do not by themselves bound sharp ratio counts near a small minimum.

There is also a source-generated continuum description of the same-shell positive levels. Under the triangular state count, $x = n/N$ and $y = r/n$ have limiting measure $2x\, dx\, dy$, and $\lambda^{(0)}/N^4 \to 9x^4y^2$. Hence $\sqrt{\lambda^{(0)}/N^4}/3$ is the product of two independent uniforms, with CDF $t(1 - \log t)$. The corresponding independent raw log-difference density is $(|d| + 2)e^{-|d|/2}/16$. This describes the disconnected raw shell spectrum, not the full finite minimum-normalized spectrum.

3.3 Adjacent shells, the minimum and signed cancellation

Let B retain all edges with $|n - m| \leq 1$, and write

$$L = B + R_g + R_c, \tag{13}$$

where R_g contains omitted edges incident on $1s$ and R_c contains the other omitted edges. Both are positive graph Laplacians. Ground-incident omitted weight is tiny relative to core weight, but it supplies most of the minimum motion. Core edges instead supply the material high-mode shifts. This separates the normalization mechanism from the bulk mechanism without removing either.

The minimum can be calculated from the source without inserting the observed target eigenvalue. On the constant complement choose the unit contrast between $1s$ and the uniform rest, and complete it orthogonally. Then

$$L_+ = \begin{pmatrix} \alpha & \xi^* \\ \xi & H \end{pmatrix}, \qquad a = \alpha - \xi^*(H - aI)^{-1}\xi. \tag{14}$$

If $H \geq gI$ with $g > \alpha$, Rayleigh's principle gives $a \leq \alpha$, and comparison with the 2×2 matrix having diagonal (α, g) and off-diagonal $\|\xi\|$ gives a lower bound. The function on the right of (14) is decreasing below g, so evaluating it at interval endpoints in reversed order and intersecting produces valid successive enclosures. A source Cholesky floor and a geometric resolvent series evaluate it without requiring a rest-spectrum diagonalization. The original-coordinate residual estimate gives a numerical minimum interval approximately $[2.05903639204, 2.05903672699]$, with the independently evaluated rest floor exceeding 17.1341. The decimal enclosure uses the stated residual and rounding model, not directed interval arithmetic.

For $F(\lambda, a) = \log\log(1 + \lambda/a)$,

$$dF = \eta(\lambda/a)(d\log\lambda - d\log a), \qquad \eta(x) = \frac{x}{(1+x)\log(1+x)}. \tag{15}$$

The function η decreases. Minimum motion therefore acts differently on low and high modes, while a pair retains only the difference of their motions. Define the full, fixed-minimum baseline and own-minimum baseline profiles by $P_0 = P(\lambda, a)$, $P_1 = P(b, a)$ and $P_2 = P(b, b_1)$. Set $E_s = P_1 - P_0$ and $E_a = P_2 - P_1$. The exact vector identity

$$P_2 - P_0 = (P_1 - P_0) + (P_2 - P_1) \tag{16}$$

must be evaluated before norms. The two terms have RMS about 2.08828×10^{-4} and 1.88192×10^{-4}; their sum has RMS 6.05482×10^{-5} and their cosine is about -0.9588. Positivity alone does not force this matching: ground-only and core-only interventions lose the strong cancellation. Common scaling $R = cB$, by contrast, cancels exactly under (10).

The fixed 16-mode predictor retains within-block mixing rather than fitting scalar shifts. Diagonalize B on the constant complement, with basis V and eigenvalues b_i, and form $A = \mathrm{diag}(b) + V^*RV$. For consecutive 16-mode projectors P_j define

$$D_{16} = \sum_j P_j A P_j. \tag{17}$$

Pool and sort the block eigenvalues, replace the first by the independently derived a, and apply the original readout and windows. The omitted cross-block matrix remains available for error control. The natural-case componentwise RMS prediction error is about 2.86437×10^{-5}. Its predicted total discrepancy, 5.96993×10^{-5}, is close to the actual discrepancy, but this

Table 1: Source-reconstructed controls for $B + gR_g + cR_c$. The Predicted, Actual and Error columns are RMS45 values in units of 10^{-4}: predicted and actual uncorrected discrepancy, and the componentwise prediction error. The last column is the cosine between the actual spectral and normalization vectors E_s, E_a in Eq. (16). These are known mathematical development controls, not unseen observations.

Control	g	c	Predicted	Actual	Error	Cosine
Natural	1	1	0.59699	0.60548	0.28644	-0.95878
Ground only	1	0	1.75233	1.75233	0.00000	0.06870
Core only	0	1	1.78978	1.66763	0.28041	-0.45157
Half ground	0.5	1	1.28992	1.18160	0.26203	-0.88356
Half core	1	0.5	0.81043	0.81514	0.19810	-0.94639
$3R_g/4 + R_c/4$	0.75	0.25	0.80785	0.79587	0.11673	-0.90226

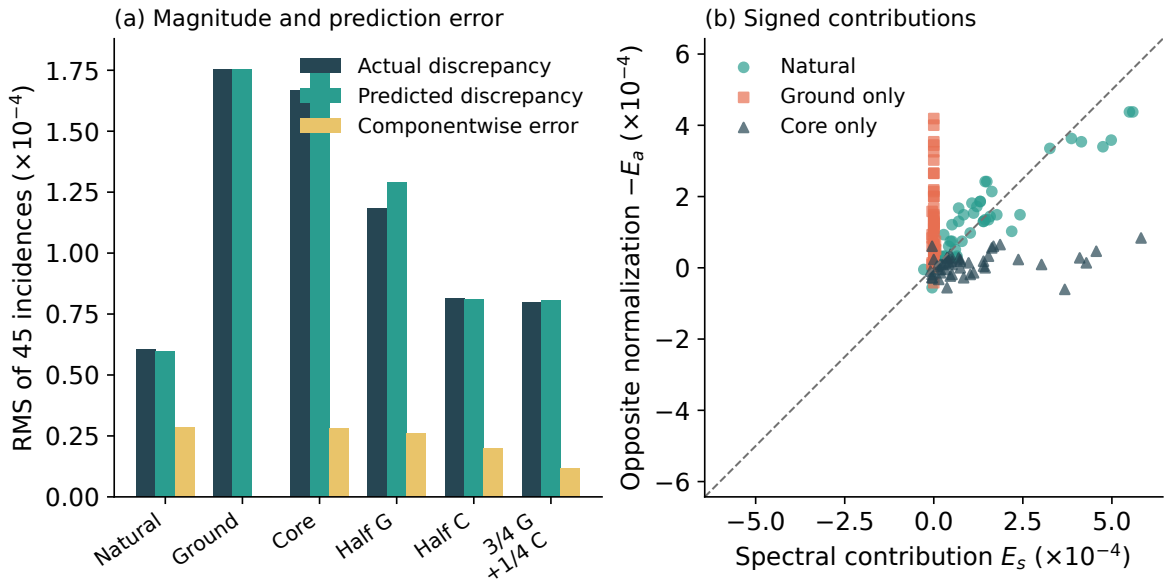


Figure 1: Executed hydrogen control calculations, generated from all 45 original coordinates. Here G and C denote the ground and core remainders. (a) The magnitude of the predicted discrepancy is distinct from the RMS error of its coordinate predictions. (b) Each point is a coordinate of the signed spectral contribution versus the opposite normalization contribution; the dashed line denotes exact cancellation. Natural mixing lies closer to this relation than either isolated remainder. No sampling uncertainty or independent empirical observation is represented.

agreement of magnitudes is a separate, weaker comparison. A full baseline eigensolve and dense source transform are still required. No computational speed advantage is inferred.

Table 1 and Figure 1 compare the fixed 16-mode predictor with direct source-graph validation for six retained controls. Ground-only mixing has almost no spectral contribution (RMS 2.08×10^{-6}) but a normalization contribution of 1.75×10^{-4}. Core-only mixing has a spectral contribution of 1.79×10^{-4} and a much smaller normalization contribution of 3.18×10^{-5}. Natural mixing combines the two roles with cosine -0.95878, producing its smaller total discrepancy. The mixed controls show how changing their balance changes cancellation. Agreement of the natural predicted and actual RMS magnitudes does not imply coordinatewise equality: the componentwise error remains 2.86437×10^{-5}. Ground-only has zero predictor error in these 45 integer count coordinates, not an asserted equality of its full eigenvalue spectrum. Every control here is previously executed mathematical development evidence. The public code regenerates the source minimum, all 45 target and predictor counts, signed components, table and figure directly from the radial graph.

3.4 Signed shell self-energies and a radial convergence bound

The local construction retains matrix blocks and spectral ranks instead of assigning perturbative eigenvectors through crossings. For an orthogonal retained projector P, put $Q = I - P$ and write the source in the B basis as $\left(\begin{smallmatrix} A_{PP} & C \\ C^* & H \end{smallmatrix}\right)$. The exact Schur matrix at real x is

$$S(x) = A_{PP} - xI - C(H - xI)^{-1}C^*. \tag{18}$$

Congruence gives $n_-(A - xI) = n_-(H - xI) + n_-(S(x))$ whenever the exterior inverse exists. Negative exterior directions contribute with their signs. Replacing every virtual contribution by a positive norm would erase the cancellation being studied.

Split the remainder by principal-shell lag, $R = R_2 + R_3 + R_{\mathrm{far}}$, with far lag at least four. Retain the full C and A_{PP}. All exterior spectra and inverses below act on $Q\mathcal{H}$, with Q as its identity; set

$$D_0 = Q(B + R_2 + R_3 - \sigma I)Q, \quad E = QR_{\mathrm{far}}Q, \quad G_0(x) = [D_0 - (x - \sigma)I]^{-1}.$$

Theorem 3.2 (Signed exterior expansion)**.** *Suppose* $\operatorname{dist}(0, \operatorname{spec} D_0) \geq g$, $|x - \sigma| \leq r < g$, *and* $\|E\| \leq \beta < d = g - r$. *Put* $\rho = \beta/d$. *For any integer* $m \geq 0$,

$$(H - xI)^{-1} = \sum_{j=0}^{m} (-G_0E)^j G_0 + \mathcal{R}_m, \qquad \|\mathcal{R}_m\| \leq \frac{\rho^{m+1}}{d(1-\rho)}. \tag{19}$$

Every retained word is selfadjoint. Congruence by C *gives a two-sided Loewner self-energy error bounded by* $\|C\|^2\rho^{m+1}/[d(1-\rho)]$. *Exterior inertia is constant throughout the window, including homotopy from* $E = 0$ *to* E.

Proof. The spectral gap gives $\|G_0\| \leq 1/d$. Factor $H - xI = (D_0 - (x - \sigma)I)(I + G_0E)$ and expand the last inverse geometrically. The remainder is $(-G_0E)^{m+1}(I + G_0E)^{-1}G_0$, with the displayed norm bound. The word $(G_0E)^jG_0 = G_0EG_0 \cdots EG_0$ equals its adjoint even though E and G_0 need not commute. The true inverse and the finite sum are selfadjoint, so their norm bound is a two-sided scalar Loewner bound. Finally $\|tE\| < d$ for $0 \leq t \leq 1$ excludes zero eigenvalues along the homotopy and throughout the window. Inertia is consequently unchanged. □

Lag-two and lag-three interference remains inside D_0 and the full coupling. The signs of its quadratic and cross terms are not universal. An independent rational fixture with indefinite $D_0 = \operatorname{diag}(-2, 3)$ and noncommuting positive E verifies the ordering and remainder

for degrees zero through seven. Endpoint rank brackets, rather than assumed monotonicity of a truncated noncommuting polynomial, return the local result to ordered eigenvalue intervals.

A radial estimate bounds the far graph before matrix compression. Let $u_{n\ell} = rR_{n\ell}$, normalized in $L^2(dr)$. Its squared radial moment is

$$M_{n\ell} = \|ru_{n\ell}\|^2 = \frac{n^2}{2}[5n^2 + 1 - 3\ell(\ell+1)]. \tag{20}$$

For each admitted adjacent angular channel k, the functions u_{mk} are orthonormal. Apply Bessel's inequality to the disjoint union of retained finite lag-at-most-three states, finite far states and the selected external states $m = 31, 32, 33$. If $\nu(\ell)$ counts the admitted adjacent channels, this proves

$$d_{\mathrm{far}}(n,\ell) \le \nu(\ell)M_{n\ell} - d_{\le 3}(n,\ell) - \sum_{\substack{m=31,32,33 \\ k \text{ admitted}}} W_{n\ell,mk}. \tag{21}$$

Only channels admitted by the finite graph are used, so an upward channel from $\ell = 29$ is not added. No continuum completeness assumption is needed. The subtracted vectors are orthogonal to the finite far subset within each channel; unused continuum or higher-shell norm only leaves nonnegative slack.

For any nonnegative weighted graph, $\|L_{\mathrm{far}}\| \le 2\max_i d_{\mathrm{far}}(i)$, by $|z_i - z_j|^2 \le 2(|z_i|^2 + |z_j|^2)$. Orthogonal compression cannot increase this norm. The coarse moment-minus-retained bound gives approximately 1.620289×10^6 and fails contraction in three of the four required sectors. The reason is concrete: large radial norm lies in channels outside the cutoff. Subtracting the three external shells in (21) gives the verified scalar upper

$$\beta = 33507.79904140163. \tag{22}$$

Exact Fraction arithmetic evaluates 2,789 retained weights and 2,697 external weights and saves every row budget. Regenerating all 8,990 original edges verifies the rounding premise and all 465 stored far-row inequalities. Under $|\widehat{W} - W| \le uW$, division by $1-u$ transfers the exact budget to the stored graph; the final floating upper is checked against that rational quantity. These scalar and edge certificates are exact. Exterior gaps, inverse residuals, products and inertia remain numerical matrix evaluations.

3.5 Returning the bound to all original counts

The six formerly unresolved windows involve 53 partner ranks. Four retained partner sectors of dimensions $96, 96, 96, 48$ give radial expansion ratios approximately 0.12183, 0.08096, 0.06291, 0.01893. Signed degrees $5, 4, 4, 3$ with widened endpoints pass 106 rank checks after charging assembly, gap, inverse-substitution, product and eigen-residual allowances. A narrower endpoint widening failed and is retained as a negative verification result. The successful return keeps actual far-edge entries in the correction words. It is a controlled finite reconstruction, not a prediction from a few scalar moments alone.

For positive spectral intervals $[\ell_i, u_i]$ and common minimum interval $[a_-, a_+]$, readout monotonicity gives

$$\log(1 + \ell_i/a_+) \le v_i \le \log(1 + u_i/a_-).$$

When extremizing a pair, the same minimum must occur in both entries. Equation (15) shows that the ratio is monotone in the common a for fixed spectral endpoints, so the shared endpoint choices suffice; the minimum mode is anchored exactly at $\log 2$. Guaranteed and possible memberships then enclose each integer count. Mixed low/high membership can equivalently use the raw threshold $a[(1 + \lambda_i/a)^q - 1]$ and source inertia. Reversing a below-one window uses reciprocal endpoints exactly, rather than a newly symmetric tolerance.

The final calculation recovers all 45 finite H30 count coordinates numerically and agrees with independent target diagonalization. Their widthwise SUM totals are 23495, 7800, 3895; the original transformed UNION totals are 21892, 7800, 3895. These quantities coincide only where the windows do not overlap. For $\sqrt{2}$, the three recovered total counts at the three tolerances are $5433, 1792, 894$; for $\log 2$, the corresponding three counts are $4858, 1621, 821$, respectively. Machine-generated tables in the supplement retain every coordinate and signed predictor error.

The costs matter to the interpretation. Partner discovery uses 1,856 cached Schur queries in addition to source setup and 106 endpoint checks. Earlier mixed-count work used thousands of full-size inertia evaluations. The radial bound adds 2,697 exact external acquisitions; its exact retained-plus-external budget uses 5,486 calls, and full stored-edge verification adds 8,990 calls. Actual far-coupling words and exterior-gap work remain. This result explains why the signed correction converges and returns the sharp finite observable, while leaving a cheaper cutoff-uniform amplitude law open.

3.6 Cutoff concentration and the informative finite tail

Theorem 3.3 (Concentration of the native comparison statistic)**.** *For the full and adjacent-shell squared-radial graphs at cutoff N, every fixed window in (6) at the three stated tolerances has incidence tending to zero as $N \to \infty$ under its own minimum-normalized readout. Their 45-coordinate RMS difference therefore tends to zero.*

Proof. Put $q = N(N+1)/2$. Both graphs dominate the same-shell direct sum. Bessel's bound (20) gives maximum degree at most $5N^4$ and hence $\lambda_{\max} \le 10N^4$. The $1s$ degree is at most three, so its centered Rayleigh vector gives $a \le C_N = 3q/(q-1)$. Call a positive mode bad if $\lambda < N^{7/2}$. By min-max and Proposition 3.1, the number of bad modes is bounded by the N shell zero modes plus the number of pairs with $9n^2r^2 < N^{7/2}$. Summing $\min(n, O(N^{7/4}/n))$ over shells shows that the bad fraction is $O(N^{-1/4}\log N) + O(N^{-1})$.

For two good modes the largest possible readout ratio is at most

$$Q_N = \frac{\log(1 + 10N^4/C_N)}{\log(1 + N^{7/2}/C_N)} \longrightarrow \frac{8}{7}.$$

Indeed the ratio for fixed numerator and denominator rates increases with a, by the decreasing elasticity in (15). Every above-one window here has lower endpoint at least $0.97\sqrt{2} > 8/7$, and every below-one upper endpoint is less than $7/8$. Eventually no good/good pair is counted. If b of $m = q - 1$ positive modes are bad, each incidence and UNION are bounded by

$$1 - \frac{(m-b)(m-b-1)}{m(m-1)} \longrightarrow 0.$$

The difference of the two finite coordinate vectors consequently tends to zero. □

This theorem explains a readout effect: the growing bulk is compressed toward pair ratio one. It does not supply the small H30 discrepancy, since the explicit finite upper bounds are loose. Finite informative tail modes, shared normalization and signed shell corrections remain essential. Agreement along a cutoff sequence alone is therefore a weaker discriminator than recovery of the actual finite amplitudes and their response to source interventions.

4 A physical dipole carrier and an operational loss readout

4.1 Angular factors and the equilibrium metric

A physical electric-dipole transition acts on $|n, \ell, m\rangle$, not on a single state per radial multiplet. Consider spinless nonrelativistic hydrogen projected to the finite manifold $n \le 30$,

with isotropic preparation within each magnetic multiplet and a weak stationary isotropic field. Write its interaction as $e\sum_a E_a(t)r_a$. In the weak-noise Markov and secular population approximation (whose use requires a specified bath and limiting regime; see 6), the rate is proportional to the field spectral density at the Bohr frequency times the squared dipole matrix element. The angular identity, with the standard Wigner $3j$ normalization [7],

$$\langle \ell' m' | C_{1q} | \ell m \rangle = (-1)^{m'} \sqrt{(2\ell+1)(2\ell'+1)} \begin{pmatrix} \ell & 1 & \ell' \\ 0 & 0 & 0 \end{pmatrix} \begin{pmatrix} \ell & 1 & \ell' \\ m & q & -m' \end{pmatrix}$$

gives, after summing final magnetic states and polarization, $A_{\ell,\ell+1} = (\ell+1)/(2\ell+1)$ and $A_{\ell,\ell-1} = \ell/(2\ell+1)$. Thus the lumped population rates are

$$q_{n\ell\to n'\ell'} = \kappa J(\omega_{n'n}) W_{n\ell,n'\ell'} A_{\ell,\ell'}. \tag{23}$$

Here κJ includes the field strength and the factors converting radial length squared into inverse seconds. Equal populations within multiplets, a valid population reduction and the finite-manifold filtering are constitutive assumptions. In particular, same-shell zero-frequency noise is retained in the flat model below; vacuum spontaneous emission is a different bath.

For a flat symmetric effective spectrum $J = 1$, put $g_i = 2\ell_i + 1$ and $c_{ij} = \max(\ell_i, \ell_j) W_{ij}$. Then $q_{ij} = \kappa c_{ij}/g_i$, so $g_i q_{ij} = g_j q_{ji}$. There are $\sum_{n=1}^{30} n^2 = 9455$ spinless magnetic states. The row generator has stationary law proportional to g, and its selfadjoint relaxation representative is

$$K_{\text{phys}} = \kappa D_g^{-1/2} L_c D_g^{-1/2}, \qquad K_{\text{phys}} \sqrt{g} = 0. \tag{24}$$

The equilibrium metric is part of this representation. A thermal bath instead retains its frequency asymmetry and Boltzmann factor, with stationary weights proportional to $(2\ell + 1)e^{-\beta E_n}$. Neither change removes the within-shell degeneracy.

Proposition 4.1 (Frequency-only bath obstruction)**.** *Under the population lumping in (23), no positive frequency-only isotropic bath spectrum makes the rates equal to a common positive multiple of the unweighted radial graph on the entire retained manifold.*

Proof. The allowed transitions $2s \to 3p$ and $2p \to 3d$ have the same Bohr frequency and nonzero radial weights. Dividing their rates by those weights gives respectively κJ and $2\kappa J/3$. Equality to one positive graph rate would require both $\kappa J = c$ and $\kappa J = 3c/2$. This is impossible. The actual squared radial weights are positive, approximately 9.39309 and 22.54342, as verified directly from the finite radial formula. Temperature or frequency dependence cannot separate two transitions sharing that frequency. □

Define $d_{\uparrow,i} = \sum_{j:\ell_j=\ell_i+1} W_{ij}$ and $d_{\downarrow,i} = \sum_{j:\ell_j=\ell_i-1} W_{ij}$, the radial row strengths in the upward and downward angular channels. What survives is a precise corrected-carrier relationship. At $\kappa = 1$,

$$K_{\text{phys}} = \tfrac{1}{2}L + E, \qquad E_{ii} = \frac{d_{\uparrow,i} - d_{\downarrow,i}}{2(2\ell_i+1)},$$

and on an edge with angular labels $\ell, \ell+1$ its negative off-diagonal coefficient relative to W_{ij} is

$$\frac{\ell+1}{\sqrt{(2\ell+1)(2\ell+3)}} = \frac{1}{2}\left(1 - \frac{1}{4(\ell+1)^2}\right)^{-1/2}.$$

The high-angular off-diagonal correction is $O(\ell^{-2})$, but low-angular states and different stationary vectors prevent treating this as a globally small relative perturbation of L. Indeed an untransported two-sided comparison $cL \le K_{\text{phys}} \le CL$ would force their kernels to agree. They do not. A positive-sector comparison must first transport the stationary direction or use

the equilibrium quotient metric. The corrected carrier's calculated native-style profile differs from H30 by RMS about 2.90337×10^{-4}, a comparison of distinct mathematical operators.

Population relaxation also does not supply a nontrivial atomic coherent face. The Hamiltonian commutator vanishes on energy-diagonal populations, and the ordinary atomic Hamiltonian does not commute with radial edges joining different n. An additional aligned complex-amplitude realization could supply a reactive symbol, as in the spatial construction below. It would be a new physical law, rather than a consequence of the Pauli equation.

4.2 Loss mixtures realize the logarithmic readout

Proposition 4.2 (Operational logarithm)**.** *For a finite positive carrier K and a calibrated $a > 0$,*

$$\log(I + K/a) = \int_0^\infty \frac{e^{-s}}{s}(I - e^{-sK/a})\, ds. \tag{25}$$

For $0 < s_0 < s_1$, let $Z = \int_{s_0}^{s_1} e^{-s}\, ds/s$ and sample age s with density $e^{-s}/(sZ)$. Multiplying the mean modal loss by Z approximates the readout. On a mode $x = \lambda/a \geq 0$ the omitted contribution is nonnegative and at most

$$xs_0 + e^{-s_1}/s_1. \tag{26}$$

Proof. For the scalar integral differentiate in x: dominated integration on compact x intervals gives $\int_0^\infty e^{-(1+x)s}\, ds = 1/(1+x)$. Its value at zero is zero, proving $\log(1+x)$. Finite spectral calculus gives (25). On the omitted lower interval use $1 - e^{-sx} \leq sx$; on the upper interval use $1 - e^{-sx} \leq 1$ and $1/s \leq 1/s_1$. Integration gives (26). □

The loss difference must be formed before integration: e^{-s}/s on the entire positive line is not a probability density. The finite choice $(s_0, s_1) = (10^{-12}, 30)$ has $Z \simeq 27.053805451$ and age dynamic range 3×10^{13}. In physical time $t = s/a$, the longest age is $30/a$ seconds when a is in inverse seconds. Numerical quadrature over the 464 positive modes of both nominated carriers preserves their original window counts; this is a deterministic integration check, not a finite-shot count guarantee.

To specify a measurement, suppose a prepared mode yields independent bounded loss outcomes $Y \in [0, 1]$ at the sampled ages. Hoeffding's inequality [8] gives

$$\Pr\{|Z\overline{Y} - \mathbb{E}(Z\overline{Y})| \geq \varepsilon\} \leq 2e^{-2M\varepsilon^2/Z^2}.$$

For m separately accessible modes, $M \geq Z^2 \log(2m/\delta)/(2\varepsilon^2)$ samples per mode suffice simultaneously with failure probability at most δ. Truncation, gap-calibration error, preparation error and detector bias must also enter the readout intervals before sharp memberships are counted. Uniform modal access, independent trials, retained loss outcomes and a calibrated clock are physical resources. The construction makes an operational interpretation possible; it does not establish that such preparation generated the historical empirical readout.

5 Spatial preparation and kernel-mass heterogeneity

5.1 A conditional Gaussian-exchange realization

Fix distinct sites $x_i \in \mathbb{R}^2$. A free-space heat mediator with diffusivity D has kernel $H(\tau, x) = (4\pi D\tau)^{-1} \exp[-|x|^2/(4D\tau)]$. Sampling its normalized influence at preparation time τ gives

$$G_{ij} = H(\tau, x_i - x_j)/H(\tau, 0) = e^{-|x_i - x_j|^2/(2\sigma^2)}, \qquad \sigma^2 = 2D\tau.$$

Hold these coefficients fixed during the subsequent response. Put $s = G\mathbf{1}$ and $L = \operatorname{diag}(s) - G$; the diagonal self terms cancel. This is exactly the complete Gaussian graph used in the spatial analysis. Setting σ to the median pair distance specifies $D\tau$, rather than deriving a universal physical diffusion time.

For complex amplitudes take $F = \kappa z^* L z/2$ with $\kappa > 0$ and scalar dissipative and reactive mobilities $\gamma > 0$, $\alpha > 0$. Its real Hessian commutes with the complex structure, giving

$$\dot{z} = -(\gamma + \mathrm{i}\alpha)\kappa L z, \qquad K_d = \gamma\kappa L, \quad C = \alpha\kappa L. \tag{27}$$

This is an exact paired CSCF realization under the declared constitutive assumptions, with $h(\lambda) = \alpha\lambda/\gamma$ on the retained finite spectrum and a bounded nondecreasing extension. The limit $\alpha = 0$ is purely dissipative and is not the nontrivial paired realization used here. The uniform stationary sector is removed by preparing $\sum_i z_i = 0$. If amplitudes have units A, then κ has energy/A^2 units and the mobilities have A^2/energy/second units. Amplitude decay is $\gamma\kappa\lambda$, phase frequency is $\alpha\kappa\lambda$, and energy decay is twice amplitude decay. Eliminating a live mediator would require its memory law; the sampled fixed network does not perform that elimination.

5.2 A finite degree-to-spectrum theorem

Theorem 5.1 (Gaussian kernel mass)**.** *Order $s_{(1)} \le \cdots \le s_{(N)}$ and the Laplacian eigenvalues $0 = \lambda_1 < \lambda_2 \le \cdots \le \lambda_N$. Then*

$$\lambda_i \le s_{(i)}, \qquad \sum_{i=1}^{N} (s_{(i)} - \lambda_i) = N.$$

The equally weighted positive spectra $\lambda_2/N, \ldots, \lambda_N/N$ and $s_{(2)}/N, \ldots, s_{(N)}/N$ have Wasserstein distance

$$W_1 = \frac{N - s_{(1)}}{N(N-1)} \le \frac{1}{N-1}. \tag{28}$$

Proof. The Fourier representation of the Gaussian makes G positive semidefinite: its quadratic form is an integral of $|\sum_j c_j e^{\mathrm{i}k\cdot x_j}|^2$ against a nonnegative Gaussian density. Hence $L \le \operatorname{diag}(s)$ and min-max gives the ordered inequalities. Since $\operatorname{tr} G = N$, trace subtraction gives their sum. All off-diagonal weights are positive, so the kernel of L consists exactly of constants. Removing its zero eigenvalue subtracts $s_{(1)}$ from the deficit. The sorted coupling is optimal for one-dimensional W_1, proving (28). □

The retained bulk is governed by kernel mass seen from a site, not by a universal topology classifier. To recover sharp windows, pair $a_i = \lambda_{i+1}$ with $b_i = s_{(i+1)}$ and define $e_i = |\log a_i - \log b_i|$. A labelled pair's log-ratio error is at most $e_i + e_j$. Its membership can change only when the predicted log-ratio lies within this distance of a window endpoint. Counting these boundary pairs bounds each incidence error. A small global spectral distance alone does not control a discontinuous window or a nearly zero mode. Saved-centroid computations verify the finite boundary inequalities for the retained spatial views.

5.3 A preparation law generates a ratio distribution

Prepare iid sites $X \sim \mathcal{N}(0, a^2 I_2)$ by harmonic confinement and quench them before measuring the network. Gaussian convolution gives

$$q(x) = \mathbb{E} e^{-|x-X|^2/(2\sigma^2)} = \frac{\sigma^2}{\sigma^2 + a^2} e^{-|x|^2/[2(\sigma^2+a^2)]}.$$

The population median pair distance satisfies $\sigma^2 = 4a^2 \log 2$. Since $|X|^2/(2a^2)$ is unit exponential,

$$\log q(X) = \text{constant} - \beta E, \qquad \beta = (1 + 4\log 2)^{-1}, \quad E \sim \text{Exp}(1). \tag{29}$$

Independent differences have density $e^{-|d|/\beta}/(2\beta)$. Thus the generated ratio density is

$$f_R(r) = \frac{1}{2\beta r} e^{-|\log r|/\beta}, \qquad r > 0. \tag{30}$$

Integrating this density over the original relative windows predicts their limiting incidences without inputting an observed eigenvalue density.

Here is the required passage from preparation to spectrum. For fixed bandwidth, conditional Hoeffding bounds [8] and a union bound give, with probability at least $1 - \delta$,

$$\max_i |s_i/N - q(X_i)| \le N^{-1} + \sqrt{\log(2N/\delta)/[2(N-1)]}.$$

The law of large numbers and Theorem 5.1 transfer the degree-law limit to L/N. Pair U-statistic consistency gives consistency of the empirical distance median because its population density is continuous and positive there. The kernel derivative in $\log \sigma$ is bounded by $2/e$, so replacing the fixed population bandwidth by that median changes all normalized degrees by a vanishing amount. The limit $q(X) > 0$ almost surely; continuous mapping gives the log-spectrum and product weak convergence gives the pair law. The removed diagonal mass vanishes and window endpoints have zero limiting mass. No independence of finite eigenvalues or overlapping pairs is assumed.

The isotropic curve matches H30's 3% slot ordering, yet its amplitudes differ. This success is a preparation-dependent mechanism for the order, rather than an identification of Gaussian preparation in hydrogen or photographs. More generally, $X \sim \mathcal{N}(0, C)$ gives

$$q(x) = \det(I + C/\sigma^2)^{-1/2} \exp[-\tfrac{1}{2} x^* (\sigma^2 I + C)^{-1} x].$$

If c_j are covariance eigenvalues and $b_j = c_j/(\sigma^2 + c_j)$, then $\log q(X) = \text{constant} - \frac{1}{2}\sum_j b_j Z_j^2$. Its variance is $\frac{1}{2}\sum_j b_j^2$; the independent log-difference characteristic function is $\prod_j (1 + b_j^2 t^2)^{-1/2}$. Only equal b_j in two dimensions give the Laplace law. Three frozen 512-site examples with covariances $(1, 1)$, $(4, 1/4)$ and $(16, 1/16)$ change profile amplitudes while retaining high rank agreement. They are synthetic checks of the preparation dependence, not independent images.

5.4 Extraction uncertainty and source-image scope

Proposition 5.2 (Matched-site displacement)**.** *If each labelled site moves by at most ε and the original median bandwidth is $\sigma > 2\varepsilon$, every edge changes by at most*

$$\delta = \min\{1, 2\varepsilon e^{-1/2}/\sigma + (2/e)|\log(1 - 2\varepsilon/\sigma)|\}.$$

Consequently $\|\Delta L\| \le 2(N-1)\delta$ and each ordered eigenvalue changes by at most this amount.

Proof. Each pair distance changes by at most 2ε, and matched order statistics imply the same bound for its median. At fixed bandwidth the kernel's radial derivative is at most $e^{-1/2}/\sigma$; its derivative in $\log \sigma$ is at most $2/e$. Split the two changes and use $\sigma' \ge \sigma - 2\varepsilon$. A signed edge-Laplacian perturbation has norm at most twice its largest absolute row-weight sum, by the edge quadratic form. Weyl's inequality completes the proof. □

If k sites are deleted at fixed bandwidth, with surviving block S, then

$$L_{SS} = L_{\text{deleted}} + \text{diag}\Big(\sum_{j \notin S} W_{ij}\Big), \qquad 0 \le L_{SS} - L_{\text{deleted}} \le kI.$$

Interlacing and Weyl give $\lambda_j - k \le \mu_j \le \lambda_{j+k}$. Re-estimating bandwidth adds at most $2(N-k-1)(2/e)|\log(\sigma'/\sigma)|$ to the operator bound. Changed dimension and pair exposure must be retained. A negative lower endpoint gives no positive-ratio guarantee.

Nine nominated displacement checks and three nominated deletion checks pass on saved embryo, galaxy and leaf coordinates. These bounds require an independently established coordinate error and site-disagreement budget before they support physical robustness. Threshold-induced births, mergers or unbounded component changes are not covered by the matched-site proposition.

The established extraction uses EXIF orientation, at most 512 pixels on the longest side without upsampling, fixed stored-sRGB luminance, strict dark thresholds, eight-connected components, inclusive area limits and a two-pixel separation rule. Saved centroids permit graph-level regeneration. Original photographs are absent from the present materials; six stable acquisition mappings remain unresolved and photographic redistribution permissions are not supplied. Pixel-level replay and physical image formation therefore remain separate questions. The small dark-embryo graph has a markedly different kernel-mass distribution and weaker hydrogen correlation. A uniformly spaced ring, by contrast, has a circulant Gaussian graph whose Fourier spectrum concentrates near its common degree, forcing the nominated away-from-one incidences to vanish with size. Geometry and preparation can therefore generate both recurrence and its absence under the same interaction kernel. Neither result establishes the physical origin, authenticity or semantic content of an image.

6 Kerr: joint angular and outgoing radial dynamics

6.1 The native selection and the source boundary problem

The gravitational selection retains spin weight $s = -2$, $\ell = 2, \dots, 6$, every $m = -\ell, \dots, \ell$, physical overtones $n = 0, 1, 2, 3$, and $a/M = 0, 0.5, 0.9$. Thus $3 \cdot 4 \sum_{\ell=2}^{6} (2\ell+1) = 540$ labelled modes. Zero-spin magnetic degeneracies retain their original multiplicities. With convention $e^{-\mathrm{i}\omega t}$, the dimensionless energy-decay rate is $\lambda = -2\,\mathrm{Im}(M\omega)$; the amplitude-decay rate is half this value. Physical rates in inverse seconds multiply by $c^3/(GM)$. The original readout and transmission time are

$$v = f_T(\lambda) = \frac{1 - e^{-T\lambda}}{T\lambda}, \qquad T = 12.115276586285876. \tag{31}$$

Here T is in GM/c^3 time units. Eligibility is the strict interval $0.05 < v_i/v_j < 5$, giving 272,049 ordered nonself pairs in the original data. There is no new mean normalization. Closed comparison windows remain distinct from this open exposure cutoff.

For $M = 1$ put $\Delta = r^2 - 2r + a^2$, $K_r = (r^2 + a^2)\omega - am$ and $\Lambda = A + a^2\omega^2 - 2am\omega$. The separated Teukolsky radial equation [9] is

$$\Delta^{-s} \frac{d}{dr}\left(\Delta^{s+1} \frac{dR}{dr}\right) + \left[\frac{K_r^2 - 2\mathrm{i}s(r-1)K_r}{\Delta} + 4\mathrm{i}s\omega r - \Lambda\right] R = 0. \tag{32}$$

Regular angular solutions determine $A(\omega)$, while ingoing horizon and outgoing infinity conditions select discrete complex poles. Leaver's continued-fraction construction [10] imposes these radiative conditions. The radial continued fraction is evaluated using the published `qnm` implementation [11]; the angular matrix and root continuation are evaluated explicitly in the supplement. Both pole parts are obtained from the joint boundary law, rather than by fitting frequency to damping.

In a spin-weighted spherical basis let X represent multiplication by $\cos\theta$. Its diagonal is $-ms/[\ell(\ell+1)]$ and its adjacent entry is

$$X_{\ell,\ell+1} = \sqrt{\frac{(\ell+1)^2-m^2}{(2\ell+3)(2\ell+1)}}\sqrt{\frac{(\ell+1)^2-s^2}{(\ell+1)^2}}.$$

The angular operator is $M_c = D - c^2X^2 + 2csX$, with $D_{\ell\ell} = \ell(\ell+1) - s(s+1)$ and $c = a\omega$. An extra row is included before forming X^2 and compressing, preserving the final diagonal contribution. Complex c makes this a nonselfadjoint problem.

6.2 Finite angular control and barrier shape

Since multiplication by $\cos\theta$ has norm at most one, the angular perturbation has norm at most $v = |c|^2 + 4|c|$. For the tail projector Q on $\ell \geq L+1$, with inverses restricted to its range,

$$d = (L+1)(L+2) - 2 - |A| - v > 0 \quad \Longrightarrow \quad \|[Q(M_c - A)Q]^{-1}\| \leq d^{-1}. \tag{33}$$

Indeed the diagonal tail inverse has norm at most $[(L+1)(L+2)-2-|A|]^{-1}$, and a Neumann series absorbs the perturbation. Schur elimination then bounds the retained correction by v^2/d. A contour certificate would additionally require the product of this bound and the retained resolvent norm to be below one on the contour. The executed cutoff and sensitivity checks do not establish that stronger condition. They provide numerical truncation evidence and a conditional tail theorem, not a rigorous enclosure of each infinite-dimensional pole.

The Schwarzschild limit exposes the generating geometry. The Regge–Wheeler potential is $V = (1-2/r)[\ell(\ell+1)/r^2 - 6/r^3]$. Near its maximum, with tortoise derivatives V_j and $\nu = n + 1/2$, the leading barrier approximation is $\omega^2 = V_0 - \mathrm{i}\nu\sqrt{-2V_2}$. The higher-order WKB construction [12] uses higher barrier derivatives to supply the asymmetry and anharmonic corrections. The retained third-order calculation improves both frequency and damping relative to the quadratic approximation and supplies the source-only Schwarzschild seeds for continuation. It remains a finite-order large-ℓ, fixed-n approximation, particularly limited at low ℓ and high retained overtones. The full rotating calculation imposes the outgoing radial law rather than substituting the local barrier approximation for it.

6.3 Branch identity and the complete numerical return

Continuation begins from those source-derived Schwarzschild seeds, not from observed rotating poles or a mode-cache lookup. At angular cutoff 20 and radial depth 1200, spin steps of 0.05 produced 540 locally accepted roots, but 14 labels disagreed materially with the retained catalogue and all 45 profile counts differed. One computed $n = 2$ root duplicated an $n = 3$ root to about 2.5×10^{-15}. A small local residual was therefore insufficient to preserve physical overtone labels.

The repair continued all families in the group $\ell = 3, \ldots, 6$, positive m, $n = 2, 3$ from computed spin 0.5 roots to 0.9, using 0.01 steps and secant prediction. It did not rescue only the discrepant labels using catalogue initial guesses. The repaired full selection reproduces all 45 counts, all three UNION counts and the original exposure. A further audit solves every one of the 45 highest-overtone spin-0.9 labels at depths 2400 and 4800, giving 90 checks. The maximum successive shifts are approximately 4.54×10^{-8} and 9.69×10^{-11}. The depth-refined full profile still agrees exactly, with maximum catalogue pole discrepancy about 5.07×10^{-12}. These are numerical reconstruction and convergence checks. They do not prove global branch uniqueness, an infinite radial-tail enclosure, or independent physical validation. The failed fixed-step profile is retained in the public diagnostic results.

6.4 The boundary-pole extension of the carrier picture

For fixed (ℓ, m, a), overtone damping increases while real frequency can decrease. On the computed rotating families all 114 nominated adjacent-overtone comparisons have this inversion. If $\lambda_j > \lambda_i$ but $\operatorname{Re}\omega_j < \operatorname{Re}\omega_i$, no nondecreasing h maps the damping carrier to those physical frequencies. Positive time-unit changes or a common frequency subtraction preserve the obstruction.

The appropriate enlarged object is the joint angular/radial outgoing problem, or a response operator retaining its frequency-dependent boundary self-energy and poles. This object supplies $(\operatorname{Re}\omega, -2\operatorname{Im}\omega)$ together. Its diagonal damping summary supports the positive readout (31) and the modular ratio representation, but is not the full nonnormal wave evolution. Thus Kerr shares the source-to-readout architecture while requiring an explicit boundary-pole extension of the commuting positive-carrier subclass. The 540 catalogue labels are numerical development data, not 540 independent black-hole experiments.

7 What ratio profiles identify, and what response adds

7.1 An exact homometric obstruction

Proposition 7.1. *The positive readout sets* $\{e^{a/100} : a \in A\}$ *and* $\{e^{b/100} : b \in B\}$, *where*

$$A = \{0, 1, 4, 10, 12, 17\}, \qquad B = \{0, 1, 8, 11, 13, 17\},$$

have identical complete ordered nonself ratio measures but are not related by common scaling or reciprocal scaling.

Proof. For both integer sets, the 15 positive pair differences are exactly $\{1, 2, \ldots, 13, 16, 17\}$, each once. The negative differences are their reflections. Exponentiation therefore gives identical 30-term ordered ratio multisets. Their equal extrema force any translation to be zero and any reflected translation to be reflection about $17/2$. Neither maps A to B. Translation and reflected translation of logarithms are precisely common scaling and reciprocal scaling of readouts. □

This obstruction survives every window statistic and fixed ratio cutoff, with conditional profiles defined whenever exposure is positive. To realize it with the hydrogen-style readout on general positive carriers, set $v_i = (\log 2)e^{a_i/100}$ and $\lambda_i = a(e^{v_i} - 1)$. Then $\min \lambda_i = a$ and $\log(1 + \lambda_i/a) = v_i$. Append a stationary zero if desired. The two carriers differ while their complete normalized ratio measures agree. This does not assert that the ambiguity occurs within the restricted H30 radial family or among actual Kerr poles; it proves that a general carrier cannot be recovered from pooled ratios alone.

One-point density is a different insufficient observable. Compare a two-value ensemble always equal to $(1, 2)$ with an ensemble equal to $(1, 1)$ or $(2, 2)$ with equal probabilities. Both have mean counting measure $\delta_1 + \delta_2$. Yet the expected ordered nonself incidence in the 3% window about two is $1/2$ for the first and zero for the second. Exposure is two in every realization. A mean density therefore does not supply the factorial pair law needed to predict correlated finite profiles.

Scale loss is exact under the native normalizations: $K \mapsto cK$ leaves minimum-normalized hydrogen values and mean-normalized spatial values unchanged. Their decay times change. A physical clock requires additional rate calibration. Kerr's fixed T is a separate convention and cannot inherit that invariance without changing its time scale.

7.2 Static elimination is not dynamical identification

The positive matrices

$$K_1 = \begin{pmatrix} 2 & 1 \\ 1 & 1 \end{pmatrix}, \qquad K_2 = \begin{pmatrix} 3/2 & 1 \\ 1 & 2 \end{pmatrix}$$

have the same retained static Schur complement, one. For $\dot{\Psi} = -K\Psi$ with initial state $(1, 0)$, their first-coordinate initial velocities are -2 and $-3/2$. Their eliminated memory kernels are e^{-t} and e^{-2t}. Static equality thus does not determine temporal response.

For a finite-dimensional generator G and an orthogonal projector P, with $\dot{\Psi} = G\Psi$, $x = P\Psi$, $z = Q\Psi$ and $Q = I - P$, variation of constants gives the exact equation

$$\begin{aligned} \dot{x}(t) = PGPx(t) + PGQe^{tQGQ}z(0) \\ + \int_0^t PGQe^{(t-u)QGQ}QGPx(u)\,du. \end{aligned} \tag{34}$$

An autonomous first-order law reproduces all source trajectories exactly if and only if $PGQ = 0$: sufficiency follows from the equation, and necessity follows by comparing initial velocities for arbitrary unresolved initial states at the same $x(0)$. This is the projected-dynamics contract of the Shadow framework. The hydrogen Schur calculation controls a spectral observable; it does not discard these temporal terms in a physical experiment.

7.3 Calibrated response as a constructive completion

For a known finite equally weighted positive spectrum define $S(t) = m^{-1}\sum_i e^{-\lambda_i t}$. For the two carriers in Proposition 7.1, with $a = 1$ and calibrated $t = 1$, the computed responses differ by about 0.00519145, although the ratio measures coincide. This single time distinguishes that nominated pair; it is not a universal one-sample reconstruction theorem.

Theorem 7.2 (Finite equal-weight response recovery)**.** *For known m, known $\tau > 0$, equal known modal weights and finite positive rates, the exact samples $S(k\tau)$ for $k = 1, \ldots, m$ determine the rate multiset including multiplicities.*

Proof. Set $x_i = e^{-\tau\lambda_i} \in (0, 1)$ and $p_k = mS(k\tau)$. Newton's identities recursively determine elementary symmetric polynomials from $e_0 = 1$ and

$$ke_k = \sum_{j=1}^{k}(-1)^{j-1}e_{k-j}p_j.$$

Consequently $z^m - e_1 z^{m-1} + \cdots + (-1)^m e_m$ is determined and has roots x_i with multiplicities. Recover $\lambda_i = -\log x_i/\tau$. □

An exact rational fixture uses $x = (1/2, 2/3, 3/4, 3/4)$, including a repeated mode. The theorem is exact but not uniformly Lipschitz stable: the pairs $a \pm \delta$ and a, a have equal first power sums and second power sums differing only by $2\delta^2$. Clustered roots can therefore require quadratically smaller response errors to resolve a split. Unknown count and weights require a different inverse problem. In particular, weights $(1, 0)$ with rates $(1, 2)$ or $(1, 3)$ produce the same entire trace e^{-t}; an unexcited mode remains invisible.

The operator recovery theorems in CSCF concern stronger inputs, such as a full calibrated transmission operator at known time, or an entire scale-dependent transform under compact-support hypotheses. They do not claim inversion from the 45 coordinates or the complete ratio measure. The present counterexamples therefore complement those theorems by identifying the information lost in pooling.

Prospective response tests must declare modal preparation weights or an independent observability argument, clock calibration, retained detector outcomes, uncertainty and drift. Even a complete response law cannot distinguish a source ontology from an unrestricted operational surrogate with exactly the same allowed record law. Discrimination must name restricted alternative physical models. The constructed completions recover nominated spectral targets, not arbitrary eigenvectors, geometry or microscopic source identity.

8 A connected source-to-readout account

The three mechanisms give concrete content to the arrows in (1). Coulomb radial rules organize a finite coupling graph into solvable shell modes, lifted shell-constant directions and signed inter-shell corrections. A minimum-normalized nonlinear readout converts their correlated motions into a small finite profile discrepancy. Gaussian spatial preparation instead controls the distribution of kernel mass, which controls the bulk Laplacian spectrum and its limiting pair law. Kerr's outgoing boundary problem jointly selects oscillation and decay through its angular and radial equations. These are positive generation results, with distinct retained information and physical assumptions.

Their common CSCF content is exact where a positive carrier, metric and declared symbol are supplied. The graph forms are finite closed curvature forms. A specified aligned amplitude law realizes both faces on the same spatial carrier. A reversible dipole-bath population law supplies a different equilibrium-weighted relaxation carrier, but supplies no nontrivial atomic phase law on populations. Kerr's damping diagonal is a positive summary with a valid readout calculus, while its physical frequency requires the enlarged boundary-pole source. The source-to-readout framework makes these joins explicit rather than identifying them by vocabulary alone.

The finite hydrogen result is stronger than a broad strength fraction or asymptotic coincidence: every original count is recovered, signed lag interference is retained and the radial bound returns to the sharp observable. Its substantial reconstruction costs identify a remaining theoretical opportunity. A useful next theorem would predict finite amplitudes from fewer radial invariants while preserving the shared minimum, ground/core distinction and sharp-window margins. A universal positivity bound cannot replace those ingredients. Similarly, rigorous Kerr pole certification would require radial-tail and global branch control in addition to the conditional angular estimate and numerical depth checks.

8.1 Discriminating observations

Several restricted physical comparisons follow directly. An isotropic frequency-only bath predicts a $3/2$ ratio of radial-normalized forward rates for $2s \to 3p$ and $2p \to 3d$, whereas the uniform radial generator predicts one. A test must control magnetic preparation, frequency selection, secular validity and detector uncertainty. It distinguishes these nominated rate models, not every engineered bath.

For a prepared Gaussian network, independently measured covariance and bandwidth predict the anisotropic log-kernel-mass law, including amplitude changes that a rank comparison can miss. A prospective spatial test should freeze the site-preparation law and extraction procedure, acquire coordinate and site-disagreement errors independently, and retain every declared window. Existing image graphs are development evidence. Original pixel bytes, reliable acquisition mappings and an image-formation model are required for stronger historical image claims.

For an aligned physical network, modal measurements can compare amplitude decay and phase frequency in the same coordinates. The law in (27) predicts a constant ratio α/γ and

common eigenvectors, including scalar action on degenerate carrier eigenspaces. A damping-only nondecreasing symbol is already excluded for the nominated Kerr inversions. For the homometric constructed pair, a calibrated survival measurement separates otherwise identical ratio data; finite response reconstruction requires the stronger access and equal-weight conditions in Theorem 7.2. Each experiment should retain loss/null outcomes, specify clock and preparation calibration, bound uncertainty and name its alternative models before outcomes are inspected.

8.2 Evidence boundaries and reproducibility

The public supplement separates fast checks of supplied source outputs from full numerical regeneration. Exact scalar fixtures, independent counters, source generation, numerical validation and same-code replay are labelled separately. The retained failed Kerr continuation and failed coarse radial budget are necessary diagnostics, not discarded production history. Machine-generated count and comparison tables preserve all coordinates, including zeros and unfavorable components. The existing library-specificity failure and readout-dependent abundance results remain unchanged.

No new image campaign, atomic experiment or black-hole observation is reported. The strongest empirical extensions depend on source-image acquisition, physical preparation and calibrated response information that are absent from the supplied records. The mathematical extensions concern cheaper finite radial laws, noisy response conditioning and rigorous outgoing pole certificates. These limitations do not weaken the proved conditional constructions; they specify the observations or theorems required to move from an explicit viable mechanism to an established physical origin.

9 Conclusion

Explicit source structure generates the nominated spectral profiles through three different routes: radial shells and shared normalization, spatial preparation and kernel-mass heterogeneity, and outgoing boundary dynamics. Quantitative return maps connect those routes to the unchanged finite ratio statistic. CSCF organizes their admissible carriers and complementary readouts, while the Shadow source-to-readout architecture specifies the realization data and information-retention conditions needed at each passage. Calibrated response adds distinctions that pooled ratios cannot retain. This account is a collection of concrete generation mechanisms, verified finite returns and discriminating observations, without a claim that recurrence establishes one microscopic law across the domains.

A Exact radial evaluation and numerical conventions

For $q = n - \ell - 1$, $p = m - k - 1$ and $s = 1/n + 1/m$, expanding the terminating Laguerre polynomials gives

$$I_{n\ell,mk} = \frac{4}{n^2 m^2}\sqrt{\frac{q!p!}{(n+\ell)!(m+k)!}}(2/n)^{\ell}(2/m)^{k} \times \sum_{i=0}^{q}\sum_{j=0}^{p}\frac{(-1)^{i+j}}{i!j!}\binom{n+\ell}{q-i}\binom{m+k}{p-j}(2/n)^{i}(2/m)^{j}\frac{(\ell+k+3+i+j)!}{s^{\ell+k+4+i+j}}. \tag{35}$$

Integer coefficient collection before rational evaluation avoids catastrophic floating cancellation. Exact squaring produces rational edge weights. The moment (20) follows from Laguerre

orthogonality and the recurrence

$$xL_q^\alpha = (2q+\alpha+1)L_q^\alpha - (q+1)L_{q+1}^\alpha - (q+\alpha)L_{q-1}^\alpha.$$

Writing $b = 2q+\alpha+1$, the L_q^α coefficient in $x^3 L_q^\alpha$ is $b^3+(q+1)(q+\alpha+1)(3b+2)+q(q+\alpha)(3b-2)$. Divide by the normalization coefficient b, multiply by $n^2/4$, and insert $q = n-\ell-1$, $\alpha = 2\ell+1$ to obtain (20).

All numerical spectra retain multiplicities and exactly one stationary graph mode. The hydrogen zero threshold is $50\epsilon_{\mathrm{mach}} N \max_i |\lambda_i|$. Spatial graphs use the larger of 10^{-12} and $10^{-12}\max_i |\lambda_i|$. Negative eigenvalues below the negative threshold or an unexpected stationary count are failures. No histogram or ratio rounding enters counting. Direct Boolean fixtures check inclusive endpoints, open eligibility boundaries, diagonal subtraction and overlapping windows.

For numerical matrix enclosures, if Q is a computed eigenvector matrix, $\|Q^*Q - I\| \le \eta < 1/2$ and $\|AQ - Q\Lambda\| \le r$, its orthogonal polar factor O obeys $\|Q - O\| \le \eta$. Consequently

$$\|A - O\Lambda O^*\| \le r + (\|A\| + \|\Lambda\|)\eta.$$

Assembly allowances and inverse residual estimates are charged separately. For an approximate inverse X with $\|I - HX\| \le \theta < 1$, $\|H^{-1}\| \le \|X\|/(1-\theta)$. These inequalities justify the numerical error model; they do not turn ordinary binary64 evaluations into a directed-rounding certificate.

B Homogeneous ring preparation

For equally spaced sites on a circle the Gaussian Gram matrix is circulant. If g_j is its first row and $s = \sum_j g_j$, the Fourier eigenvalues of L are $s - \widehat{g}_k$. Gaussian positivity gives $0 \le \lambda_k \le s$, and Theorem 5.1 gives total positive-mode deficit $N-s$. Choose $\varepsilon > 0$ so that $[1-\varepsilon, (1-\varepsilon)^{-1}]$ misses every retained matching window. At most $(N-s)/(\varepsilon s)$ positive modes lie below $(1-\varepsilon)s$. Any counted pair must touch one of those modes, so every incidence and UNION are at most

$$\min\left\{1, \frac{2(N-s)}{\varepsilon s(N-1)}\right\}.$$

At the median chord bandwidth s/N tends to a positive kernel integral. The bound is therefore $O(N^{-1})$. The homogeneous preparation removes kernel-mass heterogeneity while retaining the same complete Gaussian interaction, explaining why that preparation need not produce the nonzero limiting law of the isotropic Gaussian position ensemble.

C Verification scope and generated numerical tables

The public supplement specifies dependencies, input hashes, provenance, commands, numerical parameters and fresh output directories. Fast replay evaluates supplied finite inputs and checks scientific fixtures. Full regeneration reconstructs the nominated radial, spatial and Kerr source stages. Original photograph acquisition is externally limited, so saved-centroid reproduction is distinguished from pixel-level replay. The compact source archive contains the editable manuscript and bibliography separately from the public numerical package.

The final generated tables and executed-package verification records accompany this appendix. Values are generated from machine-readable numerical outputs rather than independently transcribed reporting tables. Finite numerical reconstruction, exact arithmetic fixtures and empirical observations retain their distinct evidence classes throughout.

Table 2: Recovered native counts generated from the retained source outputs. Hydrogen exposure is 214832; Kerr exposure is 272049. Columns retain the original widths and labelled multiplicities.

	Hydrogen			Kerr		
Centre	3%	1%	0.5%	3%	1%	0.5%
φ	2717	906	444	4523	1587	792
φ^{-1}	2709	904	444	4679	1606	791
φ^2	390	122	65	6430	2002	1016
$\sqrt{2}$	5433	1792	894	9622	4313	2403
$\sqrt{3}$	1967	658	338	7413	2457	1210
$\sqrt{5}$	657	212	107	2763	813	337
π	213	73	33	1724	577	263
$\pi/2$	3158	1051	524	2572	606	298
$\pi/10$	201	66	35	2014	658	343
e	315	104	51	9312	3757	1981
e^{-1}	314	105	52	9286	3731	1970
$\log 2$	4858	1621	821	9483	2891	1652
$j_{0,1}$	512	168	78	8528	3460	1651
3/13	51	18	9	2894	781	362
1/7	0	0	0	1951	522	295
SUM	23495	7800	3895	83194	29761	15364

Table 3: Frozen anisotropic Gaussian examples, 512 sites. Variance error refers to the population-kernel-mass plug-in diagnostic; profile RMS and rank are relative to the isotropic example.

Covariance	Variance error	RMS45	3% rank
(1, 1)	0.01750	0.0000000	1.000000
(4, 0.25)	0.01741	0.0012105	0.992857
(16, 0.0625)	0.02207	0.0013673	0.978571

References

[1] Jeremy Rodgers. Cross-domain spectral ratio structure: Refined recurrence, robustness and diagnostic limits. Unpublished manuscript, 2026.

[2] Jeremy Rodgers. The canonical spectral-curvature field: A unified operator origin for coherence, dissipation, and spectral budgets. Unpublished manuscript, 2026.

[3] Jeremy Rodgers. Source–readout non-equivalence: Descent and equivariant reconstruction obstructions. Unpublished manuscript, 2026.

[4] Jeremy Rodgers. Geometric realization of completed source relations. Unpublished manuscript, 2026.

[5] Jeremy Rodgers. Observable quotients and exact projected dynamics: Closure, memory, minimal dynamical completion, and effective field operators. Unpublished manuscript, 2026.

[6] E. B. Davies. Markovian master equations. *Communications in Mathematical Physics*, 39:91–110, 1974. doi: 10.1007/BF01608389.

[7] National Institute of Standards and Technology. Digital Library of Mathematical Functions, Section 34.3: Basic Properties of 3j Symbols, n.d. URL https://dlmf.nist.gov/34.3. Accessed 3 November 2026.

[8] Wassily Hoeffding. Probability inequalities for sums of bounded random variables. *Journal of the American Statistical Association*, 58(301):13–30, 1963. doi: 10.1080/01621459.1963.10500830.

[9] Saul A. Teukolsky. Perturbations of a rotating black hole. i. fundamental equations for gravitational, electromagnetic, and neutrino-field perturbations. *The Astrophysical Journal*, 185:635–647, 1973. doi: 10.1086/152444.

[10] E. W. Leaver. An analytic representation for the quasi-normal modes of kerr black holes. *Proceedings of the Royal Society of London. Series A*, 402(1823):285–298, 1985. doi: 10.1098/rspa.1985.0119.

[11] Leo C. Stein. qnm: A python package for calculating kerr quasinormal modes, separation constants, and spherical-spheroidal mixing coefficients. *Journal of Open Source Software*, 4(42):1683, 2019. doi: 10.21105/joss.01683. URL https://joss.theoj.org/papers/10.21105/joss.01683.

[12] Sai Iyer and Clifford M. Will. Black-hole normal modes: A wkb approach. i. foundations and application of a higher-order wkb analysis of potential-barrier scattering. *Physical Review D*, 35:3621, 1987. doi: 10.1103/PhysRevD.35.3621.